Phonon-limited valley life times in single-particle bilayer graphene quantum dots

L. Banszerus,[1,2,*] K. Hecker,[1,2,*] L. Wang,[3] S. Möller,[1,2] K. Watanabe,[4]
T. Taniguchi,[5] G. Burkard,[3] C. Volk,[1,2] and C. Stampfer[1,2]

[1] *JARA-FIT and 2nd Institute of Physics, RWTH Aachen University, 52074 Aachen, Germany, EU*
[2] *Peter Grünberg Institute (PGI-9), Forschungszentrum Jülich, 52425 Jülich, Germany, EU*
[3] *Department of Physics, University of Konstanz, 78457 Konstanz, Germany, EU*
[4] *Research Center for Electronic and Optical Materials, National Institute for Materials Science, 1-1 Namiki, Tsukuba 305-0044, Japan*
[5] *Research Center for Materials Nanoarchitectonics, National Institute for Materials Science, 1-1 Namiki, Tsukuba 305-0044, Japan*

(Dated: February 27, 2024)

The valley degree of freedom in honeycomb crystals such as 2D semiconductors, graphene and bilayer graphene is a promising carrier of quantum information alongside spin and charge. This is all the more true since gate-controlled single-particle quantum dots (QDs) have been demonstrated in bilayer graphene (BLG), paving the way for the realisation of spin and valley qubits. Although long spin relaxation times have recently been reported in BLG QDs, nothing is known about single-particle valley lifetimes. Here we report single-particle valley relaxation times (T_1 times) exceeding several microseconds in electrostatically defined BLG QDs. The observed dependence of T_1 on the perpendicular magnetic field can be understood qualitatively and quantitatively by a model in which T_1 is limited by electron-phonon coupling. We identify coupling to acoustic phonons via the bond length change and via the deformation potential as the limiting mechanisms.

Bernal-stacked BLG comes as a gapless semimetal, where electrons and holes can be described as massive Dirac fermions [1]. However, when applying an out-of-plane electric displacement field D, the inversion symmetry of the crystal lattice is broken, as the on-site energy of carbon atoms of the top layer becomes different from that of the atoms of the bottom layer (see Fig. 1a) [2]. This leads to the opening of a band gap at the two valleys, K and K' (see Fig. 1b), which depends on the strength of the symmetry breaking potential, i.e., on D [3–5], resulting in a highly tunable band structure that allows for gate-defined charge carrier confinement [6–8]. The broken inversion symmetry also leads to a finite Berry curvature, Ω, near the K points, where Ω has opposite signs at the K and K' points and has mirror symmetry for electrons and holes [2, 9] (see Fig. 1c). The Berry curvature gives rise to a valley-dependent anomalous velocity term leading to the valley-Hall effect in extended BLG samples [10, 11] and to finite out-of-plane magnetic moments in BLG QDs. These topological orbital magnetic moments, which have opposite signs for K and K', couple to an external out-of-plane magnetic field and are the origin of the valley Zeeman effect in BLG QDs [12, 13].

To successfully create gate-defined QDs in BLG, the electronic wave function needs to be confined by a potential $U(\mathbf{r})$ in real space (see Fig. 1a) and will be distributed near the K and K' points, in k-space. A single-electron or single-hole QD can then be described by the Hamiltonian $H_{\mathrm{QD}} = H_{\mathrm{BLG}} + H_{\mathrm{Z}} + H_{\mathrm{SO}} + U(\mathbf{r})$ [14]. Here, H_{BLG} represents the effective 4×4 Hamiltonian of bulk BLG near the K- and K'-points based on the sublattice and layer degrees of freedom and includes the bulk valley Zeeman effect (see Methods), which will be further modified by the confinement $U(\mathbf{r})$. H_{Z} denotes the spin Zeeman coupling. H_{SO} describes the intrinsic Kane-Mele spin-orbit (SO) coupling, which lifts the zero B-field degeneracy of the four single-particle states, leading to the formation of two Kramers' pairs with opposite spin and valley quantum numbers, ($|K\uparrow\rangle$,$|K'\downarrow\rangle$) and ($|K'\uparrow\rangle$, $|K\downarrow\rangle$), separated by the SO gap, Δ_{SO}. In BLG quantum devices Δ_{SO} has typically values in the range of $40 - 80$ μeV [7, 9, 12, 15, 16]. In Fig. 1d we show the single-particle spectrum of a BLG hole QD as function of the out-of-plane magnetic field, $B_\perp$. As $B_\perp$ couples to both the spin and the valley magnetic moments, we observe linear energy shifts given by $E(B_\perp) - E(0) = (\pm g_{\mathrm{s}} \pm g_{\mathrm{v}})\mu_{\mathrm{B}} B_\perp/2$ [17]. Here, μ_{B} is the Bohr magneton, $g_{\mathrm{s}} \approx 2$ is the spin g-factor and the valley g-factor, g_{v}, quantifies the strength of the Berry-curvature induced valley magnetic moment, which can be tuned by the confinement potential of the QD in a range typically between $g_{\mathrm{v}} \approx 10$ and 70 [13, 18]. All this makes the valley degree of freedom well accessible and allows significant valley polarisation at reasonably small $B_\perp$-fields (see separation of $|K'\rangle$ and excited $|K\rangle$ states in Fig. 1d).

The fabricated device used to confine single charge carriers in a BLG QD is depicted by the scanning electron micrograph in Fig. 2a. The QD device consists of a flake of BLG encapsulated by two crystals of hexagonal boron nitride (hBN) and placed on a graphite flake acting as a back gate. On top of the van-der-Waals heterostructure, metallic split gates (SGs) are used to gap out the BLG underneath the SG areas, resulting in a narrow n-type conductive channel connecting the source and drain leads (see contacts in Fig. 2a). To confine charge carriers, the band edge profile along the channel can be adjusted

* These authors contributed equally to this work

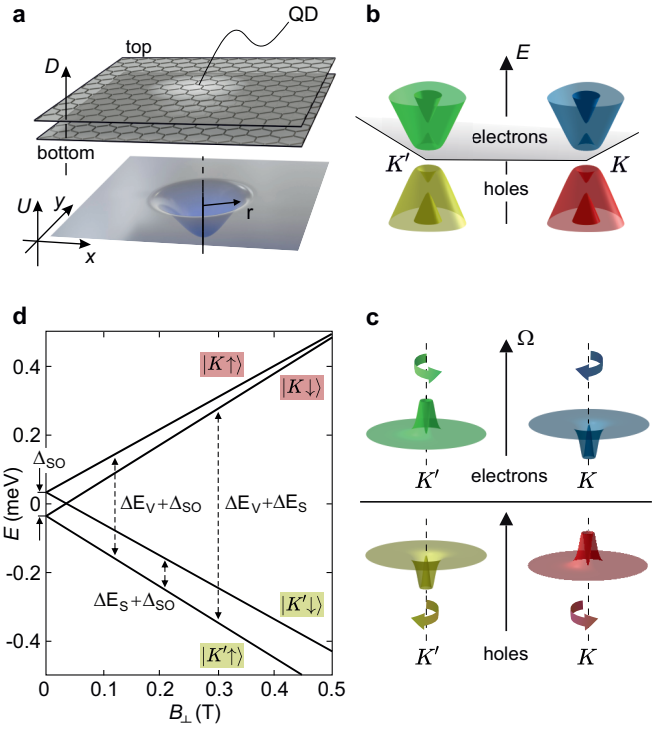

FIG. 1. Electrostatically defined single-particle QD in BLG. **a** Lattice structure of bilayer graphene highlighting the top and bottom layer and a symmetry breaking displacement field, D. The electrostatic confinement potential U (shown in the lower panel) allows to form a QD. **b** Band structure of gapped BLG. Close to the K (blue/red) and the K' (green/yellow) valley a band gap opens. **c** The broken inversion symmetry results in a finite Berry curvature, Ω, near the K and K' points, which has opposite sign for the two valleys and for electrons and holes. **d** Single-particle spectrum of a BLG QD. At $B_\perp = 0$, the four states are grouped into two spin and valley unpolarized Kramers' doublets split by the Kane Mele SO gap, $\Delta_{\rm SO}$. A finite $B_\perp$ couples to both the spin and valley magnetic moments, resulting in a spin and valley Zeeman effect, leading to additional energy splittings of $\Delta E_{\rm s} = g_{\rm s}\mu_{\rm B}B$ and $\Delta E_{\rm v} = g_{\rm v}\mu_{\rm B}B$. The arrows depict the transition energies between the ground state $|K'\uparrow\rangle$ and the three excited states.

using two layers of interdigitated finger gates (FGs) [6, 8]. One of the FGs is used as a plunger gate (PG) to tune the QD (see red FG in Fig. 2a) and allows to locally overcompensate the channel potential set by the back gate. The width of the PG measures about 70 nm and the separation of the SGs is around 80 nm, which set an upper limit of the QD radius r to around 30 to 40 nm. The DC potential applied to the plunger gate, $V_{\rm PG}$, allows to control the charge carrier occupation of the QD down to the last hole (see Fig. 2b). Additionally, to study transient transport through the QD, an AC potential, $V_{\rm AC}$, can be applied to the PG via a bias tee (see Fig. 2a). To maximize the transient currents and to study the relaxation dynamics of the QD states, the FGs adjacent to the PG are used to reduce the tunnel coupling between the QD and the left and right reservoir, $\Gamma_{\rm L}$ and $\Gamma_{\rm R}$, respectively (see colored FGs in Fig. 2a) [19–22].

To study the relaxation dynamics of an excited valley state, we first investigate the single-particle spectrum of the QD. For that purpose, we perform excited state transient current spectroscopy measurements by applying a square pulse with a frequency, f, (duty cycle 50%) to the PG (see Fig. 2c and Methods for details). Fig. 2d shows the average number of charge carriers that are tunneling through the QD per pulse cycle, $\langle n\rangle/\text{pulse} = I/(fe)$, with the elementary charge e, as a function of the pulse amplitude, $V_{\rm AC}$, and the DC plunger gate voltage, $\Delta V_{\rm PG}$, relative to the Coulomb peak position at $V_{\rm AC} = 0$. The pulse frequency has been fixed at $f = 5$ MHz and the magnetic field at $B_\perp = 300$ mT. At finite $V_{\rm AC}$, transport via the ground state (GS) may occur when the GS resides within the bias window during either part of the square pulse ($\tau_{\rm i}, \tau_{\rm m}$), resulting in a splitting of the GS Coulomb peak ($|K\uparrow\rangle_i$ and $|K\uparrow\rangle_m$) [20, 23]. Once $V_{\rm AC}$ becomes large enough such that an excited state (ES) enters the bias window, a transient current via the ES contributes to the overall current and shows up as a resonance in Fig. 2d (see coloured dashed lines). From the positions of the two prominent ES resonances in Fig. 2d, we can extract their corresponding ES energies (see Methods) and measurements as shown in Fig. 2d have been recorded for various $B_\perp$-fields. Fig. 2e depicts the energy difference between the ground state ($|K'\uparrow\rangle$) and the first spin ES (yellow data points, $|K'\downarrow\rangle$) and the valley ESs, (red data points $|K\downarrow\rangle$, $|K\uparrow\rangle$) as a function of $B_\perp$. The energy splitting of the spin ES and the GS increases linearly with $B_\perp$ due to the spin Zeeman effect. A fit to the data yields a spin g-factor of $g_{\rm s} = 2.0 \pm 0.2$ and a zero-field splitting of $\Delta_{\rm SO} = 75$ μeV in agreement with the slightly proximity-enhanced Kane-Mele SO coupling [9, 12, 15]. Due to the finite peak width, the energy of the two valley ESs cannot be determined independently. Thus, the data has been fit considering the average energy splitting with a slope corresponding to $g_{\rm v} + g_{\rm s}/2$. A valley g-factor of $g_{\rm v} = 30.2 \pm 0.2$ has been determined, similar to values reported in earlier works [12, 13].

Next, we investigate the relaxation dynamics of the observed single-particle valley ES. For that purpose, we apply a three-level pulse scheme to the PG and measure the tunneling current through the QD [21]. The pulse scheme, depicted in Fig. 3a, is characterized by the lengths of each pulse step ($\tau_{\rm i}$, $\tau_{\rm h}$ and $\tau_{\rm m}$) and the corresponding voltages ($V_{\rm i}$, $V_{\rm h}$ and $V_{\rm m}$). During $\tau_{\rm i}$, the QD is initialized in the empty state. Subsequently, during $\tau_{\rm h}$, the GS $|K'\uparrow\rangle$, the spin ES $|K'\downarrow\rangle$ and the two valley ESs $|K\uparrow\rangle$ and $|K\downarrow\rangle$ are tuned below the electrochemical potentials of the source and drain leads. After the characteristic tunneling time on the order of $1/(\Gamma_{\rm L}+\Gamma_{\rm R})$ either the GS or one of the three ESs will be occupied by a single charge carrier. A charge carrier in an ES has the chance to relax into an energetically lower lying state by either spin or valley relaxation with a characteristic relaxation time, T_1. Finally, during $\tau_{\rm m}$, we perform a val-

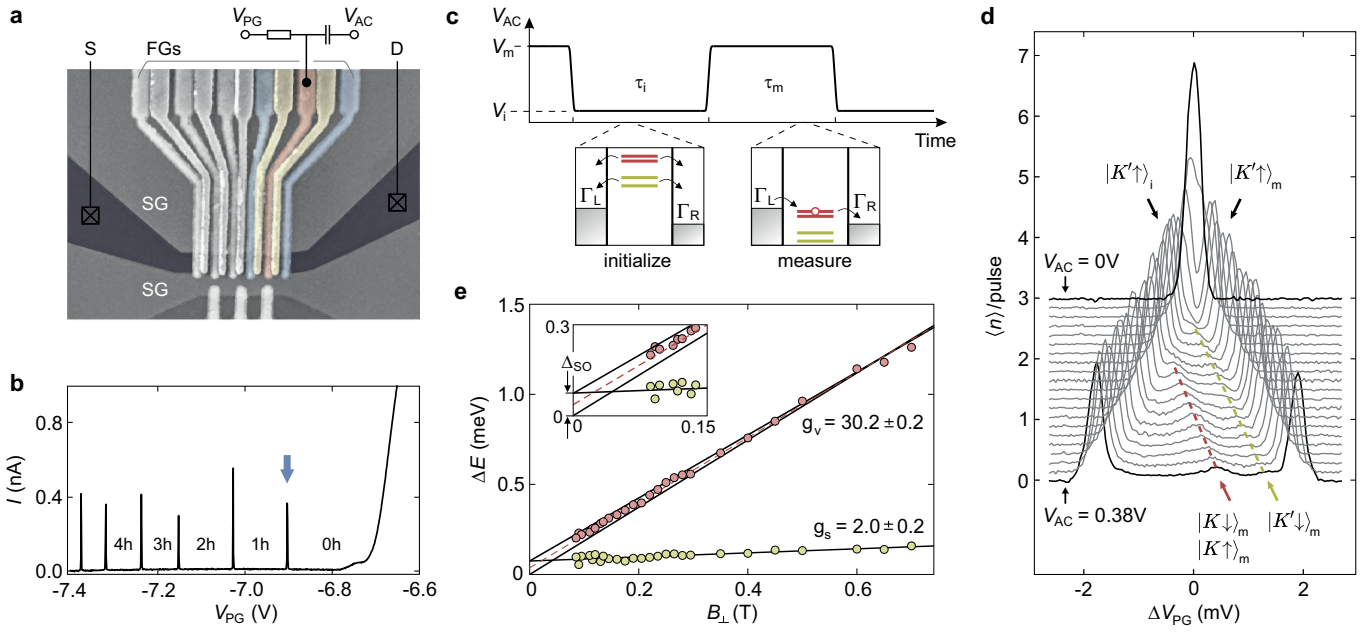

FIG. 2. BLG quantum dot device and measurement of the single-particle spectrum. **a** False-colored scanning electron microscopy image of the gate structure of the device. A channel is formed between source (S) and drain (D) using two split gates (SGs). The potential along the channel is controlled using two layers of finger gates (FGs). One FG (red) is used as a plunger gate (PG) for the QD, while the neighboring FGs (yellow and blue) are used to tune the tunneling barriers between the QD and the reservoirs. The PG is connected to a bias tee for applying AC and DC signals to the same gate. **b** Current through the device as function of $V_{\rm PG}$ at a source-drain bias voltage of $V_{\rm SD} = 200\ \mu$V. The n-type channel is pinched off close to $V_{\rm PG} = -6.8V$. Upon further decreasing $V_{\rm PG}$, a hole QD is formed, and Coulomb resonances appear when additional holes are added to the QD (see labels). **c** Top: Schematic of the square pulse applied to the PG which is characterized by the voltages $V_{\rm i}$ and $V_{\rm m}$ and the times $\tau_{\rm i}$ and $\tau_{\rm m}$. Bottom: Schematic of the QD states relative to the electrochemical potentials of the leads. **d** Excited state (ES) spectroscopy using transient current measurements. The average number of charge carriers $\langle n \rangle$ tunneling through the QD per pulse is plotted as function of $\Delta V_{\rm PG}$ for different $V_{\rm AC}$. Traces are offset for clarity. Current via the ground state $|K'\uparrow\rangle$ occurs at $\Delta V_{\rm PG} = 0$ mV. Orange and yellow arrows and dashed lines highlight transient currents via excited states ($|K'\downarrow\rangle$, $|K\uparrow\rangle$ and $|K\downarrow\rangle$). **e** Energy ΔE of the ES relative to the GS as a function of $B_\perp$. From a fit to the energy of the spin ES (yellow), $\Delta_{\rm SO}$ and $g_{\rm s}$ is extracted, while a fit according to $\Delta_{\rm SO}/2 + (g_{\rm v} + g_{\rm s}/2)\mu_{\rm B}B$ (orange dashed line) yields $g_{\rm v}$. The solid lines indicate the energies of the valley ESs deduced from the fits. The inset shows a close-up of the low-$B_\perp$ regime.

ley selective readout measured by aligning the $|K\rangle$ states in the bias window. Only charge carriers occupying one of the two $|K\rangle$ states, which have not relaxed into a $|K'\rangle$, can tunnel out and contribute to the transient current.

Fig. 3b shows the current, I, through the QD as a function of $V_{\rm PG}$ while applying the pulse sequence depicted in Fig. 3a. The three peaks labeled $|K'\uparrow\rangle_{\rm i}$, $|K'\uparrow\rangle_{\rm h}$ and $|K'\uparrow\rangle_{\rm m}$ correspond to GS transport during each of the three pulse steps. Furthermore, transient currents via the three ESs, $|K\uparrow\rangle_{\rm m}$, $|K\downarrow\rangle_{\rm m}$ and $|K'\downarrow\rangle_{\rm m}$, can be observed during $\tau_{\rm m}$. The relaxation time T_1 of $|K\uparrow\rangle$ into an energetically lower lying state can be probed by measuring the amplitude of the $|K\uparrow\rangle_{\rm m}$ peak as a function of the holding time $\tau_{\rm h}$ [19, 21, 22]. We convert the current I into the number of charge carriers tunneling through the QD per pulse cycle, $\langle n\rangle/\text{pulse} = I(\tau_{\rm i} + \tau_{\rm h} + \tau_{\rm m})/e$. The number of charge carriers $\langle n\rangle_{|K\uparrow\rangle_{\rm m}}$ tunneling via the ES $|K\uparrow\rangle_{\rm m}$, is directly proportional to the probability of $|K\uparrow\rangle$ remaining occupied after $\tau_{\rm h}$, $P_{|K\uparrow\rangle}(\tau_{\rm h})$. The relative occupation probability of $|K\uparrow\rangle$ as a function of $\tau_{\rm h}$ decays exponentially with the characteristic relaxation time, T_1 [19, 21]:

$$\frac{\langle n\rangle_{|K\uparrow\rangle_{\rm m}}(\tau_{\rm h})}{\langle n\rangle_{|K\uparrow\rangle_{\rm m}}(0)} = \frac{P_{|K\uparrow\rangle}(\tau_{\rm h})}{P_{|K\uparrow\rangle}(0)} = e^{-\tau_{\rm h}/T_1}. \qquad (1)$$

Fig. 3c depicts $P_{|K\uparrow\rangle}(\tau_{\rm h})/P_{|K\uparrow\rangle}(0)$ as function of $\tau_{\rm h}$ for three different out-of-plane magnetic fields. All three datasets show an exponential decay of the occupation probability as a function of $\tau_{\rm h}$. From an exponential fit (solid line), we determine for example $T_1 = 4.0\ \mu$s at $B_\perp = 0.175$ T. T_1 decreases with increasing $B_\perp$ and reaches a value of 845 ns at $B_\perp = 0.45$ T. A single charge carrier occupying $|K\uparrow\rangle$ may relax into a lower lying state either by pure valley relaxation ($|K\uparrow\rangle \rightarrow |K'\uparrow\rangle$) or by additionally flipping the spin ($|K\uparrow\rangle \rightarrow |K'\downarrow\rangle$). Relaxation processes requiring a single valley flip are expected to be faster than processes that require both a spin and valley flip. This is supported by the fact that spin relaxation times between hundreds of microseconds to up to 50 ms have been recently reported in BLG [21, 22]. Hence, we conclude that T_1 extracted from Fig. 3c must be limited by the valley relaxation time. In Fig. 4, we

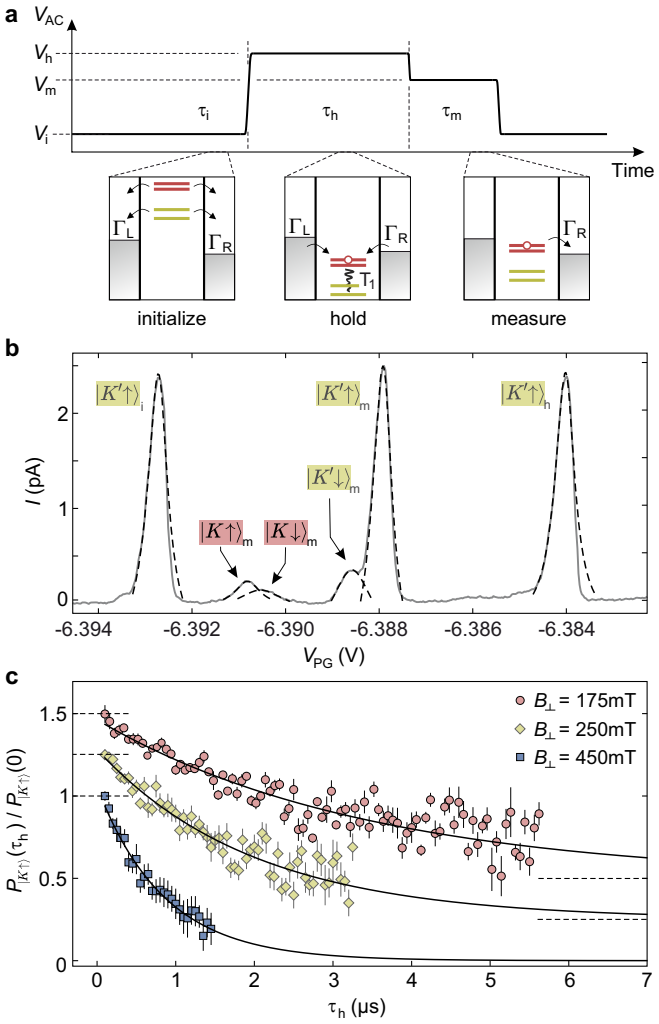

FIG. 3. Measurement of the valley relaxation time. **a** Top: Schematic of the three-level pulse scheme applied to the PG which is characterized by the voltages V_i, V_h and V_m and the times τ_i, τ_h and τ_m. Bottom: Schematic of the QD states relative to the electrochemical potentials in the leads (see text for details). **b** Current I as a function of V_{PG} while the pulse sequence in **a** is applied. The valley T_1 time is derived from the amplitude of $|K\uparrow\rangle_m$. Dashed curves are Lorentzian fits to the peaks. The measurement has been taken at $B_\perp = 0.22$ T and $V_{SD} = 10$ μV. **c** Relative occupation probability of $|K\uparrow\rangle$ after the holding pulse, $P_{|K\uparrow\rangle}(\tau_h)/P_{|K\uparrow\rangle}(0)$ as a function of the holding time, τ_h. Data has been taken at $B_\perp = 0.175$, 0.25 and 0.45 T, respectively. The traces are offset for clarity.

plot the valley relaxation time T_1 (data points) extracted from exponential fits, as exemplarily shown in Fig. 3c as a function of $B_\perp$ and as a function of the energy splitting ΔE_v. When decreasing $B_\perp$ from 0.7 T to about 0.15 T, T_1 increases from below 0.5 μs to about 7 μs, while at even lower $B_\perp$, the relaxation rate decreases again to $T_1 \sim 2$ μs at 80 mT (see gray data points).

To gain a better understanding of the experimental T_1 results, we compare them with theory and therefore model the system by the Hamiltonian $H = H_{QD} + H_{EPC} + H_{KK'}$, where H_{QD} describes a single electron or hole in the BLG QD and $H_{EPC} = \sum_{\lambda q} H_{EPC}^{\lambda q}$ the electron-phonon coupling. Furthermore, we allow a mixing between the two valleys described by the intervalley coupling term $H_{KK'} = \Delta_{KK'}\tau_x/2$ where τ_x is the Pauli matrix acting on the valley degree of freedom. For simplicity, the electrostatic confinement is modeled by a finite circularly symmetric step potential $U(\mathbf{r})$ with potential depth $U_0 \approx 39.6$ meV and QD radius $r = 25$ nm. This yields a valley g-factor of $g_v = 30$, which is in good agreement with the experimental data (c.f. Fig. 2e). We consider transitions between states with equal spin, but opposite valley degree of freedom mediated by coupling to in-plane acoustic phonons arising either from the deformation potential (characterized by the coupling strength g_1) or from bond-length change (coupling strength g_2) [24]. The Hamiltonian describing coupling to phonons in the mode λ with wave vector q has the form $H_{EPC}^{\lambda q} = c_q(g_1 a_1 \sigma_0 + g_2 a_2' \sigma_x + g_2 a_2'' \sigma_y)(e^{i\mathbf{q}\cdot\mathbf{r}} b_{\lambda q}^\dagger - e^{-i\mathbf{q}\cdot\mathbf{r}} b_{\lambda q})$ with $\sigma_{x,y,z}$ the Pauli matrices for the sublattice degree of freedom [25, 26], and $c_q = \sqrt{q/A\rho v_\lambda}$, with A the area of the BLG sheet, ρ the mass density of BLG, and v_λ the sound velocity; $a_{1,2}$ are phase factors and $b_{\lambda q}$ and $b_{\lambda q}^\dagger$ are the phonon ladder operators [14]. Using Fermi's golden rule, we calculate the valley relaxation times T_1 between initial and final eigenstates $|i\rangle$ and $|f\rangle$ of the Hamiltonian $H_{QD} + H_{KK'}$ with opposite valley quantum number and eigenenergies ε_i and ε_f,

$$\frac{1}{T_1} = 2\pi A \sum_\lambda \int \frac{d^2q}{(2\pi)^2} |\langle i| H_{EPC}^{\lambda q} |f\rangle|^2 \delta(\varepsilon_f - \varepsilon_i + v_\lambda q). \tag{2}$$

We only take into account the emission of phonons (with energy $v_\lambda q$) as the thermal energy is significantly smaller than the valley splitting. To quantify the electron-phonon coupling strength, we perform the least square fit to the experimental data using g_1 and g_2 as free fit parameters. Our model is in good qualitative and quantitative agreement with the data taken above $B_\perp = 0.1$ T, where increasing $B_\perp$ results in decreasing T_1, while it cannot explain the decrease in T_1 observed for $B_\perp < 0.1$ T, suggesting that other mechanisms dominate T_1 in this regime. We speculate that the discrepancy between our model and the data in this regime may arise from a hot spot [27] or charge noise [28, 29]. Consequently, we have restricted the fit to the data taken for $B_\perp \geq 0.1$ T. The fit yields coupling parameters of $g_1 = 50$ eV, $g_2 = 5.4$ eV. It is noteworthy that both parameters are in good agreement with the reported literature values, which include values in the range of 20 to 50 eV for g_1 [30–34] and values in the range of 1.5 to 5 eV for g_2 [24, 34], where the wide range of values is partly due to the dependence of the deformation potential on screening and doping [30, 31]. The black solid line in Fig. 4 corresponds to the contributions from both, the deformation potential coupling and from bond length change coupling, while the blue and red dashed lines show the individual contributions,

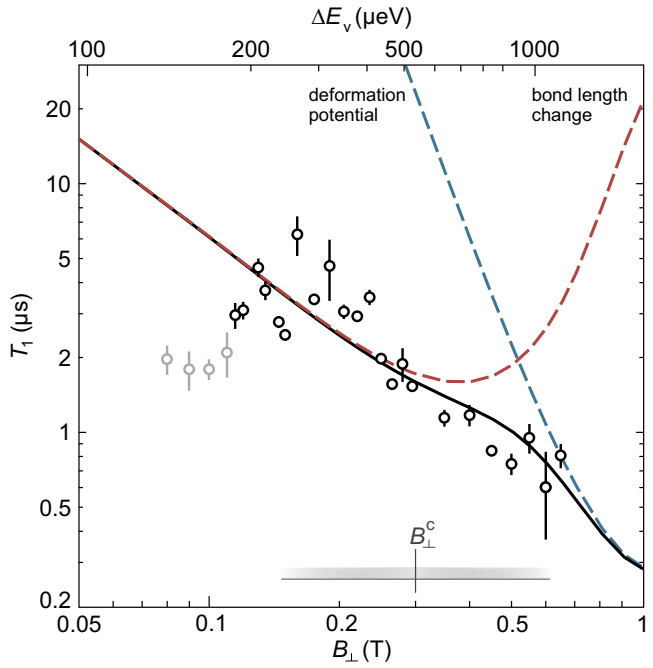

FIG. 4. Dependence of T_1 on the valley splitting. Valley relaxation time T_1 as a function of the applied $B_\perp$ (bottom axis) and the valley splitting $\Delta E = g_v \mu_B B_\perp$ (top axis). The error bars indicate the 1σ confidence interval of an exponential fit to the data as shown in Fig. 3c. The black curve represents a fit to the experimental data, assuming T_1 to be limited by electron-phonon coupling arising from the deformation potential and from bond length change. The fit neglects the first four data points and yields coupling parameters $g_1 = 50$ eV, $g_2 = 5.4$ eV. The blue (red) curve shows the contribution of the deformation potential (bond length change) separately. The critical field $B_\perp^c$ marks the crossover between the dipole and the higher multipole regime.

respectively (see labels in Fig. 4). In the calculation, the intervalley coupling, which is mainly responsible for the absolute T_1 values but does not enter the functional $B_\perp$ dependence, was set to $\Delta_{KK'} = 50$ μeV.

At larger magnetic fields, $B_\perp \gtrsim 0.5$ T, T_1 is predominantly limited by electron-phonon coupling via the deformation potential, whereas at smaller fields it is limited by the coupling due to bond length change. This transition occurs due to the crossover between the dipole and the higher multipole regimes for the bond-length change coupling if the phonon wavelength $\lambda \approx 2\pi\hbar v_\lambda/(g_v \mu_B B_\perp)$ is comparable to the QD radius r, where $qr = 2\pi r/\lambda \approx 1$. Hence, the crossover occurs around the critical field $B_\perp^c \approx \hbar v_\lambda/(g_v \mu_B r) \approx 0.3$ T. The assumed QD radius of $r = 25$ nm is in agreement with the lithographic device dimensions as well as with the confinement size giving rise to a valley g-factor of $g_v = 30$ in excellent agreement with experiment. The gray horizontal bar in Fig. 4 depicts the range of $B_\perp^c$ assuming the estimate of r to deviate by a factor of 2 highlighting that the transition region is well within the experimentally investigated B-field range.

The long single-particle valley lifetimes in BLG QDs of up to 7 μs demonstrated by our work confirms that the valley degree of freedom is indeed an interesting candidate for implementing qubits. This potential is furthermore underlined by a recent experiment showing long relaxation times from valley triplet to valley singlet states [35]. By fitting to the experimental data, we confirm that over a wide magnetic field range, electron-phonon coupling mediated by bond length change and the deformation potential limit the relaxation time. As the valley magnetic moment is typically one to two orders of magnitude larger than the magnetic moment associated with the electron spin, we anticipate gate operation times of a valley qubit to be much faster than those of a spin qubit, potentially compensating for the shorter relaxation times. The magnitude of the valley magnetic moment can be adjusted all-electrically, which could provide a way to realize control over a single valley without the need for microwave bursts, micromagnets or ESR strips, and enable well-controlled qubit addressability. A crucial follow-up experiment is the determination of coherence times (T_2^* and T_2) in this system, potentially using a recently demonstrated particle electron-hole blockade as a readout method [9].

Methods

The device is composed of a van-der-Waals heterostructure, where a BLG flake is encapsulated between two hBN flakes of approximately 25 nm thickness and placed on a graphite flake which acts as a back gate (BG). Cr/Au split gates on top of the heterostructure define a 80 nm wide channel. Across the channel, two layers of interdigitated Cr/Au finger gates of 70 nm width, are fabricated. Two 15 nm thick layers of atomic layer deposited (ALD) Al_2O_3 act as gate dielectric. For details of the fabrication process, we refer to Ref. [36].

In order to perform RF gate modulation, the sample is mounted on a home-built printed circuit board (PCB). All DC lines are low-pass-filtered (10 nF capacitors to ground). All FGs are connected to on-board bias-tees, allowing for AC and DC control on the same gate (see Fig. 2a). All AC lines are equipped with cryogenic attenuators of -26 dB. V_{AC} refers to the AC voltage applied prior to attenuation. The measurements are performed in a ^{3}He/^{4}He dilution refrigerator at a base temperature of approximately 20 mK and at an electron temperature of around 60 mK. The current through the device is amplified and converted into a voltage with a home-built I-V converter at a gain of 10^8. Throughout the experiment, a constant back gate voltage of $V_{BG} = 5.025$ V and a split gate voltage of $V_{SG} = -5.435$ V is applied to define a n-type channel between source and drain. The four gates acting as barrier gates to the QD (see Fig. 2a, yellow and blue color coding) are biased with -6.05 ± 0.1 V, -4.95 V, -5.18 V and -6.15 ± 0.1 V, respectively. The voltages are adjusted to compensate for the influence of $B_\perp$ on the tunnel coupling.

The Hamiltonian H_{BLG} describing the band structure of bulk BLG is given by

$$H_{\mathrm{BLG}}(\mathbf{k}) = \begin{bmatrix} \Delta & \gamma_0 p & \gamma_4 p* & \gamma_1 \\ \gamma_0 p* & \Delta & \gamma_3 p & \gamma_4 p* \\ \gamma_4 p & \gamma_3 p* & -\Delta & \gamma_0 p \\ \gamma_1 & \gamma_4 p & \gamma_0 p* & -\Delta \end{bmatrix} \quad (3)$$

with the displacement field 2Δ and the hopping parameters $\gamma_0 = 2.6$ eV, $\gamma_1 = 0.339$ eV, $\gamma_3 = 0.28$ eV and $\gamma_4 = -0.14$ eV. The momentum $p(\mathbf{k}) = -\sqrt{3}a(\tau k_x - ik_y - ixB_\perp e/2 - \tau y B_\perp e/2)/2$ with the valley index $\tau = \pm 1$ and the lattice constant $a = 2.46$ Å includes the valley Zeeman effect [2, 37, 38].

Acknowledgements
The authors thank A. Hosseinkhani for fruitful discussions and F. Lentz, S. Trellenkamp, M. Otto and D. Neumaier for help with sample fabrication. This project has received funding from the European Union's Horizon 2020 research and innovation programme under grant agreement No. 881603 (Graphene Flagship) and from the European Research Council (ERC) under grant agreement No. 820254, the Deutsche Forschungsgemeinschaft (DFG, German Research Foundation) under Germany's Excellence Strategy - Cluster of Excellence Matter and Light for Quantum Computing (ML4Q) EXC 2004/1 - 390534769, through DFG (STA 1146/11-1), and by the Helmholtz Nano Facility [39]. K.W. and T.T. acknowledge support from the JSPS KAKENHI (Grant Numbers 20H00354 and 23H02052) and World Premier International Research Center Initiative (WPI), MEXT, Japan. L.W. and G.B. acknowledge support from DFG Project No. 425217212, SFB 1432.

Data availability
The data supporting the findings are available in a Zenodo repository under accession code XXX.

Author contributions
C.S. designed and directed the project; L.B., K.H., S.M. fabricated the device, L.B., K.H. and C.V. performed the measurements and analyzed the data. K.W. and T.T. synthesized the hBN crystals. L.W. and G.B. performed calculations of the T_1 time. G.B., C.V. and C.S. supervised the project. L.B., K.H., L.W., G.B, C.V. and C.S. wrote the manuscript with contributions from all authors. L.B. and K.H. contributed equally to this work. Correspondence should be addressed via e-mail to luca.banszerus@rwth-aachen.de

Competing interests
The authors declare no competing interests.

[1] K. S. Novoselov, E. McCann, S. V. Morozov, V. I. Fal'ko, M. I. Katsnelson, U. Zeitler, D. Jiang, F. Schedin, and A. K. Geim, Nat. Phys. **2**, 177 (2006).
[2] E. McCann and M. Koshino, Rep. Prog. Phys. **76**, 056503 (2013).
[3] J. B. Oostinga, H. B. Heersche, X. Liu, A. F. Morpurgo, and L. M. K. Vandersypen, Nat. Mater. **7**, 151 (2008).
[4] Y. Zhang, T.-T. Tang, C. Girit, Z. Hao, M. C. Martin, A. Zettl, M. F. Crommie, Y. R. Shen, and F. Wang, Nature **459**, 820 (2009).
[5] E. Icking, L. Banszerus, F. Wörtche, F. Volmer, P. Schmidt, C. Steiner, S. Engels, J. Hesselmann, M. Goldsche, K. Watanabe, T. Taniguchi, C. Volk, B. Beschoten, and C. Stampfer, Adv. Electron. Mater. **8**, 2200510 (2022).
[6] M. Eich, F. Herman, R. Pisoni, H. Overweg, A. Kurzmann, Y. Lee, P. Rickhaus, K. Watanabe, T. Taniguchi, M. Sigrist, T. Ihn, and K. Ensslin, Phys. Rev. X **8**, 031023 (2018).
[7] L. Banszerus, B. Frohn, T. Fabian, S. Somanchi, A. Epping, M. Müller, D. Neumaier, K. Watanabe, T. Taniguchi, F. Libisch, B. Beschoten, F. Hassler, and C. Stampfer, Phys. Rev. Lett. **124**, 177701 (2020).
[8] L. Banszerus, B. Frohn, A. Epping, D. Neumaier, K. Watanabe, T. Taniguchi, and C. Stampfer, Nano Lett. **18**, 4785 (2018).
[9] L. Banszerus, S. Möller, K. Hecker, E. Icking, K. Watanabe, T. Taniguchi, F. Hassler, C. Volk, and C. Stampfer, Nature **618**, 51 (2023).
[10] Y. Shimazaki, M. Yamamoto, I. V. Borzenets, K. Watanabe, T. Taniguchi, and S. Tarucha, Nat. Phys. **11**, 1032 (2015).
[11] M. Sui, G. Chen, L. Ma, W.-Y. Shan, D. Tian, K. Watanabe, T. Taniguchi, X. Jin, W. Yao, D. Xiao, and Y. Zhang, Nat. Phys. **11**, 1027 (2015).
[12] L. Banszerus, S. Möller, C. Steiner, E. Icking, S. Trellenkamp, F. Lentz, K. Watanabe, T. Taniguchi, C. Volk, and C. Stampfer, Nat. Commun. **12**, 5250 (2021).
[13] C. Tong, R. Garreis, A. Knothe, M. Eich, A. Sacchi, K. Watanabe, T. Taniguchi, V. Fal'ko, T. Ihn, K. Ensslin, and A. Kurzmann, Nano Lett. **21**, 1068 (2021).
[14] L. Wang and G. Burkard, Manuscript in preparation..
[15] A. Kurzmann, Y. Kleeorin, C. Tong, R. Garreis, A. Knothe, M. Eich, C. Mittag, C. Gold, F. K. de Vries, K. Watanabe, T. Taniguchi, V. Fal'ko, Y. Meir, T. Ihn, and K. Ensslin, Nat. Commun. **12**, 6004 (2021).
[16] C. Tong, A. Kurzmann, R. Garreis, W. W. Huang, S. Jele, M. Eich, L. Ginzburg, C. Mittag, K. Watanabe, T. Taniguchi, K. Ensslin, and T. Ihn, Phys. Rev. Lett. **128**, 067702 (2022).
[17] A. Knothe and V. Fal'ko, Phys. Rev. B **98**, 155435 (2018).
[18] S. Möller, L. Banszerus, A. Knothe, C. Steiner, E. Icking, S. Trellenkamp, F. Lentz, K. Watanabe, T. Taniguchi, L. I. Glazman, V. I. Fal'ko, C. Volk, and C. Stampfer, Phys. Rev. Lett. **127**, 256802 (2021).
[19] R. Hanson, B. Witkamp, L. M. K. Vandersypen, L. H. W. van Beveren, J. M. Elzerman, and L. P. Kouwenhoven, Phys. Rev. Lett. **91**, 196802 (2003).
[20] L. Banszerus, K. Hecker, E. Icking, S. Trellenkamp, F. Lentz, D. Neumaier, K. Watanabe, T. Taniguchi,

C. Volk, and C. Stampfer, Phys. Rev. B **103**, L081404 (2021).
[21] L. Banszerus, K. Hecker, S. Möller, E. Icking, K. Watanabe, T. Taniguchi, C. Volk, and C. Stampfer, Nat. Commun. **13**, 3637 (2022).
[22] L. M. Gächter, R. Garreis, J. D. Gerber, M. J. Ruckriegel, C. Tong, B. Kratochwil, F. K. de Vries, A. Kurzmann, K. Watanabe, T. Taniguchi, T. Ihn, K. Ensslin, and W. W. Huang, PRX Quantum **3**, 020343 (2022).
[23] T. Fujisawa, Y. Tokura, and Y. Hirayama, Phys. Rev. B **63**, 081304(R) (2001).
[24] T. Sohier, M. Calandra, C.-H. Park, N. Bonini, N. Marzari, and F. Mauri, Phys. Rev. B **90**, 125414 (2014).
[25] T. Ando, J. Phys. Soc. Jpn. **74**, 777 (2005).
[26] E. Mariani and F. von Oppen, Phys. Rev. Lett. **100**, 076801 (2008).
[27] C. H. Yang, A. Rossi, R. Ruskov, N. S. Lai, F. A. Mohiyaddin, S. Lee, C. Tahan, G. Klimeck, A. Morello, and A. S. Dzurak, Nat. Commun. **4**, 2069 (2013).
[28] P. Huang and X. Hu, Phys. Rev. B **89**, 195302 (2014).
[29] A. Hosseinkhani and G. Burkard, Phys. Rev. B **104**, 085309 (2021).
[30] C.-H. Park, N. Bonini, T. Sohier, G. Samsonidze, B. Kozinsky, M. Calandra, F. Mauri, and N. Marzari, Nano Lett. **14**, 1113 (2014).
[31] E. Mariani and F. von Oppen, Phys. Rev. B **82**, 195403 (2010).
[32] J.-H. Chen, C. Jang, S. Xiao, M. Ishigami, and M. S. Fuhrer, Nat. Nanotechnol. **3**, 206 (2008).
[33] E. H. Hwang and S. Das Sarma, Phys. Rev. B **77**, 115449 (2008).
[34] H. Suzuura and T. Ando, Phys. Rev. B **65**, 235412 (2002).
[35] R. Garreis, C. Tong, J. Terle, M. J. Ruckriegel, J. D. Gerber, L. M. Gächter, K. Watanabe, T. Taniguchi, T. Ihn, K. Ensslin, and W. W. Huang, Nat. Phys. , 1 (2024).
[36] L. Banszerus, A. Rothstein, T. Fabian, S. Möller, E. Icking, S. Trellenkamp, F. Lentz, D. Neumaier, K. Watanabe, T. Taniguchi, F. Libisch, C. Volk, and C. Stampfer, Nano Lett. **20**, 7709 (2020).
[37] S. Konschuh, M. Gmitra, D. Kochan, and J. Fabian, Phys. Rev. B **85**, 115423 (2012).
[38] L. Wang and M. W. Wu, Phys. Rev. B **87**, 205416 (2013).
[39] W. Albrecht, J. Moers, and B. Hermanns, Journal of Large-Scale Research Facilities **3**, 112 (2017).